


2025 Q2

RESEARCH ARTICLE

Synergistic Effect of Bovine Serum Albumin–Gold Nanoclusters Against Antibiotic-Resistant Bacterial Sustainability and Biofilm Fabrication

Mana A. Alanazi¹ | Ramachandran Samivel¹  | Turki Almubrad¹ | Adnan A. Khan¹ | Ali Masmali¹ | Saud A. Alanazi¹ | Saeed Akhtar²

¹Cornea Research Chair, Department of Optometry, College of Applied Medical Sciences, King Saud University, Riyadh, Saudi Arabia | ²College of Applied Medical Sciences, Inaya Medical Sciences, Riyadh, Saudi Arabia

Correspondence: Ramachandran Samivel (rkumari@ksu.edu.sa) | Saeed Akhtar (sakhtar@inaya.edu.sa)

Received: 11 March 2025 | **Revised:** 24 November 2025 | **Accepted:** 24 November 2025

Keywords: antibiotic resistance | biofilm | bovine serum albumin–gold nanoclusters | microbial susceptibility | transmission electron microscope

ABSTRACT

This study evaluated the antimicrobial and antibiofilm effects of bovine serum albumin–gold nanoclusters (BSA–GNCs) against planktonic and antibiotic-resistant bacteria. BSA–GNCs were synthesized and characterized using UV spectrofluorimetry, Fourier transform infrared spectroscopy (FTIR), zeta sizing, scanning electron microscopy (SEM)–energy-dispersive x-ray (EDX), and transmission electron microscopy (TEM) analyses. Cytotoxicity was evaluated using the MTT assay. Antimicrobial and antibiofilm activities were assessed against four bacterial strains: *Klebsiella pneumoniae*, *Staphylococcus aureus*, *Pseudomonas aeruginosa*, and *Enterococcus faecalis*. A characteristic UV absorption peak at 500 nm, along with a visible color change, confirmed successful GNC formation. FTIR spectra showed prominent functional groups at 598.33, 1102.79, 1261.21, 1637.84, 2923.54, and 3430.76 cm^{−1}, and the mean hydrodynamic diameter measured 22.72 nm. BSA–GNC exposure induced moderate cytotoxicity in HaCaT cells at concentrations above 40 µg/µL. Treatment with 40 µg/µL BSA–GNCs significantly enhanced bacterial growth inhibition zones (KP: 28 ± 2.44 mm; SA: 27.5 ± 2.45 mm; PA: 31.5 ± 1.91 mm; EF: 29.75 ± 2.5 mm) after 24 h. TEM imaging of BSA–GNC-treated bacteria revealed shrunken, disrupted cells with degenerated cytoplasm. Additionally, BSA–GNC treatment markedly reduced biofilm formation at both 24 and 48 h compared with untreated controls. These findings indicate that BSA–GNCs enhance reactive oxygen species (ROS) accumulation, leading to impaired bacterial growth and biofilm formations.

1 | Introduction

Antimicrobial drugs have been widely used for decades to prevent the growth of bacteria, fungi, viruses, and other microorganisms. Although antibiotic resistance is a natural evolutionary process, the uncontrolled and inappropriate use of antibiotics in various sectors such as medicine, agriculture, animal husbandry, and the food industry has significantly reduced their effectiveness and accelerated the emergence of multidrug-resistant (MDR) pathogens [1]. In recent years, drug-resistant microorganisms

have become a major public health concern, causing pneumonia, bloodstream infections, post-COVID complications, and other severe infections that contribute to increased mortality rates [2]. According to the World Health Organization (WHO), antibiotic resistance ranks among the top ten global health threats. Several bacterial species such as *Klebsiella pneumoniae* (CRKP), *Staphylococcus aureus* (MRSA), *Pseudomonas aeruginosa* (CRPA), and *Mycobacterium tuberculosis* (MDR-TB) are listed among the most critical antibiotic-resistant pathogens [3]. Furthermore, these organisms can complicate or survive medical procedures such

as surgeries, organ transplants, and the use of medical implants, including ventilators, catheters, cardiac stents, contact lenses, orthopedic probes, and dental devices [4, 5].

Over the past few decades, antibiotic resistance has escalated into a global crisis, with hospitals serving as major reservoirs for drug-resistant bacteria. Consequently, treating device-related secondary infections has become increasingly challenging and costly, largely due to prolonged antibiotic therapies and the persistence of resistant strains. Infections associated with medical implants can arise through various routes, and antibiotic exposure itself often contributes to increased rates of implant rejection and surgical failure. To address these challenges, researchers have increasingly turned to nanotechnology as a promising alternative therapeutic approach [6–8]. Nanoparticles possess unique physicochemical properties such as high surface area, tunable surface chemistry, and diverse mechanisms of action that distinguish them from bulk materials and make them particularly suitable for combating bacterial infections.

In addition to improving drug delivery, nanoparticles can penetrate bacterial biofilms and effectively reach infection sites, thereby enhancing antibiotic efficacy [7]. Numerous studies have shown that metal-based nanoparticles exert antimicrobial effects by inducing membrane damage, generating reactive oxygen species (ROS), and causing protein dysfunction, ultimately leading to bacterial cell death [7, 8]. For example, silver (Ag-NPs) and selenium (Se-NPs) nanoparticles have been shown to inhibit the growth of MDR Gram-negative bacteria in the lower respiratory tracts of patients with chronic lung disease [9]. Similarly, Ag-NPs inhibit the growth of carbapenem-resistant *K. pneumoniae* [10]. A comparative in vitro study by Kattumuri et al. demonstrated that gold nanoparticles (AuNPs) offer superior biocompatibility and photostability compared to silver nanoparticles, without inducing cytotoxicity in human cells [11]. Likewise, Wang et al. reported that AuNPs can form a variety of nanostructures such as rods, tubes, spheres, crystals, and stars which enhance their antibacterial activity through strong electrostatic interactions between Au^+ ions and bacterial surfaces [12].

Gold nanoparticles (AuNPs), when integrated into biomedical implant surfaces, exhibit strong antibacterial activity. The primary mechanism involves electrostatic adsorption of AuNPs onto the negatively charged bacterial cell membrane. This interaction facilitates binding to lysine residues on membrane proteins, resulting in irreversible pore formation and subsequent loss of membrane integrity. Following membrane disruption, internalized AuNPs further impair bacterial viability by decreasing intracellular adenosine triphosphate (ATP) levels. The reduction in ATP disrupts essential metabolic pathways, leading to metabolic failure and cell death [13]. Bovine serum albumin–gold nanoclusters (BSA–GNCs) have gained increasing attention for diverse biomedical applications, including antibacterial therapy, chemosensing, cellular and extracellular imaging, biosensing, and radiosensitization [14–16]. Javed et al. reported that capping agents improve nanoparticle biodegradability, biocompatibility, and stability, enhancing cellular uptake while preventing aggregation [17]. BSA (~66 kDa) is particularly suitable as a capping agent because it contains multiple reactive functional groups (carboxyl, sulfhydryl, and amino groups). Previous studies have shown that BSA–GNCs enhance the bioavailability of AuNPs,

facilitating cellular uptake via surface receptors and improving nanoparticle stability, conjugation, and biocompatibility [18, 19].

Therefore, the aim of this study was designed to synthesize and characterize BSA–GNCs and to evaluate their antimicrobial, antibiofilm, and cytocompatibility efficacy against antibiotic-resistant and non-resistant bacterial strains. Additionally, the study aimed to investigate the morphological and ultrastructural alterations induced by BSA–GNC treatment to elucidate the mechanisms underlying their biofilm-inhibitory activity.

2 | Materials and Methods

2.1 | Chemicals

BSA, MTT (3-(4,5-dimethylthiazol-2-yl)-2,5-diphenyltetrazolium Bromide), and 2',7'-dichlorodihydrofluorescein diacetate ($\text{H}_2\text{DCFH-DA}$) were obtained from Life Technologies (USA). Hydrogen tetrachloroaurate (III) hydrate ($\text{HAuCl}_4 \cdot 3\text{H}_2\text{O}$) was purchased from Sigma-Aldrich (St. Louis, MO, USA). The human adult keratinocyte (HaCaT) cell line was obtained from the American Type Culture Collection (ATCC, USA). Syringe filtration membranes, dialysis membranes (Sartorius Stedim Biotech, Göttingen, Germany), and other analytical-grade reagents were also procured. For electron microscopy analyses (scanning electron microscopy [SEM] and transmission electron microscopy [TEM]), carbon-coated copper grids and related accessories were acquired from TABB Bioscience (UK). Bacterial culture media, including M63 medium, Luria–Bertani (LB) broth, Nutrient broth, and MacConkey broth/agars were obtained from Scharlab (Barcelona, Spain).

2.2 | Synthesis of BSA–GNCs

BSA-stabilized GNCs were synthesized following the method described by Purohit and Singh [20], with slight modifications. Briefly, 5 mL of BSA (65 mg/mL) and 5 mL of 10 mM chloroauric acid ($\text{HAuCl}_4 \cdot 3\text{H}_2\text{O}$; Sigma-Aldrich, St. Louis, MO, USA) were mixed thoroughly, followed by the addition of 200 μL of 1 M sodium hydroxide (NaOH). The resulting solution was stirred continuously at 40°C for 24 h. The color of the reaction mixture changed from light yellow (Figure 1A) to brown (Figure 1B), indicating the formation of BSA–GNCs. The successful synthesis of BSA–GNCs was confirmed by UV–visible spectrofluorometric analysis (Figure 1D) and by observing a red fluorescence under UV illumination (Figure 1C). The obtained BSA–GNCs were purified by dialysis using a 20 kDa molecular weight cutoff membrane against 2 L of 10 mM phosphate-buffered saline (PBS, pH 7.4) for 24 h, with PBS replaced every 6 h. The resulting solution was considered as a 1× BSA–GNC stock and stored at 4°C until further characterization.

2.3 | UV-Spectrofluorimetric Analysis

The fluorescence properties of BSA and BSA–GNCs were analyzed using a multimode microplate reader (Infinite 200, Tecan, Australia). Samples were loaded into a 96-well microplate in quintuplicate. The fluorescence emission spectra were recorded

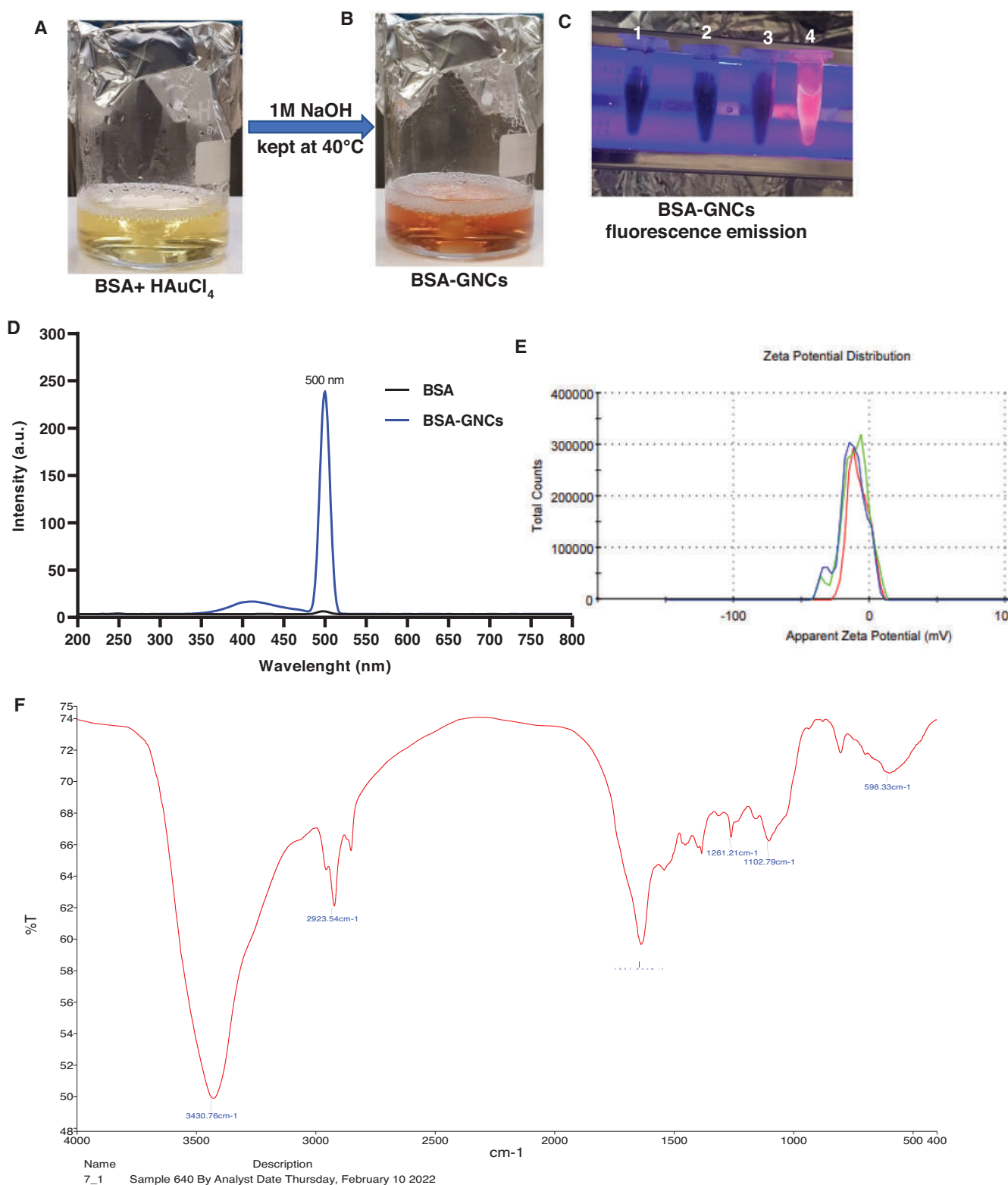


FIGURE 1 | Synthesis and characterization of BSA-gold nanoclusters (BSA-GNCs). (A) The initially prepared BSA-HAuCl₄ solution appeared light yellow; (B) after overnight stirring at 40°C, the color changed to brownish, indicating the formation of BSA-GNCs; (C) the tube containing BSA-GNCs emitted red fluorescence under a UV lamp; (D) ultraviolet-spectrofluorimetric spectrum showing the fluorescent emission peaks of BSA-GNCs; (E) zeta potential size distribution graph of the BSA-GNCs; (F) FTIR spectra demonstrating BSA interaction with the gold nanocluster surface. The prepared BSA-GNCs concentration was 1× per volume. BSA-GNCs, bovine serum albumin-gold nanoclusters.

in the wavelength range of 300–720 nm to determine the emission peak. Excitation and emission wavelengths were optimized by performing a wavelength scan analysis.

2.4 | Characterization of BSA–GNCs

The particle size distribution and spectral characteristics of the synthesized BSA–GNCs were analyzed using dynamic light scattering (DLS) and Fourier transform infrared spectroscopy (FTIR). The hydrodynamic particle size distribution was determined using a particle size analyzer (NANOPHOX, Sympatec, Attica, Greece; Figure 1E). For FTIR analysis (Figure 1F), 2 mg of BSA–GNCs was thoroughly mixed with 100 mg of potassium bromide (KBr) powder and compressed into thin pellets using a pelletizer. The FTIR spectra were recorded in the range of 400–4000 cm^{-1} with a resolution of 1 cm^{-1} using an FTIR spectrometer (PerkinElmer RX-I, Shelton, CT, USA).

2.5 | Electron Microscopy Analysis

The morphological characteristics of the synthesized BSA–GNCs were examined using SEM (JSM-6360, JEOL, Tokyo, Japan) operated at an accelerating voltage of 7.5 kV. A drop of the BSA–GNC suspension was vacuum-dried on a graphite stub prior to imaging. Elemental composition analysis was performed using an energy-dispersive x-ray spectrometer (EDS; Oxford INCA, Gujarat, India) attached to the SEM. TEM (JEOL 1400, Tokyo, Japan) was employed to determine the particle size and structural details of the BSA–GNCs. For TEM imaging, the BSA–GNC suspension was ultrasonicated and deposited onto a Formvar-coated copper grid. The particle size was measured and analyzed using iTEM software. The TEM micrographs were digitally color-coded according to particle size (Figure 2B,C).

2.6 | Cytotoxicity Assay

Human adult keratinocyte cell line (HaCaT; RRID: CVCL_0038) was obtained from the American Type Culture Collection (ATCC, USA). The cytotoxicity of BSA–GNCs was assessed using the MTT assay on HaCaT cells at passage 12. The assay was performed following the procedure described by Lillo et al. [21], with minor modifications. HaCaT cells were exposed to a range of BSA–GNC concentrations (1–100 $\mu\text{g}/\mu\text{L}$) for 24 h. After treatment, cell viability was quantified using the MTT dye to evaluate the cytotoxic potential of the BSA–GNCs.

2.7 | Bacterial Strains and Culture Conditions

The bacterial strains *K. pneumoniae* (ATCC 700603), *S. aureus* (ATCC 43300), *P. aeruginosa* (ATCC 27582), and *Enterococcus faecalis* (ATCC 29212) were obtained from the Department of Microbiology, King Saud University. The bacterial cultures were grown overnight at 37°C in LB broth (Scharlab S.L., Spain). The cells were then harvested, washed with PBS, and the turbidity of the bacterial suspension was adjusted by measuring the optical density at 600 nm (OD_{600}) using a spectrophotometer (Genesys 10S, Thermo Scientific, Waltham, MA, USA).

2.8 | Antibacterial Activity Assay

Nutrient agar medium was prepared by dissolving 5 g of peptone, 3 g of beef extract, and 5 g of sodium chloride (NaCl) in 1000 mL of distilled water, and the pH was adjusted to 7.0. Agar (15 g) was added to the medium, which was then sterilized in a conical flask under a pressure of 150 lbs for 30 min. The sterilized medium was poured into Petri dishes under aseptic conditions in a laminar airflow chamber and allowed to solidify. The bacterial strains (*K. pneumoniae*, *S. aureus*, *P. aeruginosa*, and *E. faecalis*) were inoculated onto the agar surface. The antibacterial activity of the test samples of 40 $\mu\text{g}/\mu\text{L}$ of 1× BSA–GNCs, 20 $\mu\text{g}/\mu\text{L}$ of penicillin–streptomycin (PS), BSA, and gold (Au) solutions was evaluated using the disc diffusion method following standard procedures. The inoculated plates were incubated at 37°C for 24 h, after which the diameter of the inhibition zones was measured in millimeters (mm) using a standard scale.

2.9 | Biofilm Formation and Quantification Assay

The biofilm formation assay was conducted according to the method described by O'Toole [22], with slight modifications. All four bacterial strains (*K. pneumoniae*, *S. aureus*, *P. aeruginosa*, and *E. faecalis*) were inoculated in LB broth and incubated overnight at 37°C with shaking at 120 rpm. Before initiating the assay, fresh M63 medium (provided by the Department of Microbiology, King Saud University) was used to resuspend the bacterial cultures, which were then washed with PBS to adjust turbidity. The bacterial suspensions were diluted in M63 medium to obtain a final concentration of 1×10^8 CFU/mL. Aliquots of 200 μL of the diluted bacterial cultures were transferred into the wells of a flat-bottomed 96-well microplate and incubated at 37°C for 24 and 48 h in the presence of BSA–GNCs (40 $\mu\text{g}/\mu\text{L}$). Untreated cultures served as controls. Following incubation, one set of cultures was harvested to measure the optical density at 600 nm (OD_{600}) using a spectrophotometer (Genesys 10S, Thermo Scientific, Waltham, MA, USA).

For biofilm quantification, the remaining wells were gently inverted to remove planktonic cells and rinsed several times with sterile water to remove unattached bacteria. The plates were then stained with 150 μL of 0.1% (w/v) crystal violet solution (Sigma-Aldrich, St. Louis, MO, USA) for 15 min at room temperature. Excess dye was removed by washing the plates three to four times with distilled water, followed by air-drying overnight. The stained biofilms were photographed to visually assess biofilm formation (Figure 6A,B). For quantitative analysis, 200 μL of 30% (v/v) acetic acid was added to each well to solubilize the bound crystal violet, and the plates were incubated for 15 min. The resulting solution was transferred to cuvettes, and the absorbance was measured at 550 nm (A_{550}). Each experiment was performed in triplicate, with six replicates per condition. Quantitative biofilm formation was expressed as the ratio of A_{550} (biofilm biomass) to OD_{600} (bacterial growth), normalized to the control cultures.

2.10 | Intracellular ROS Detection

Intracellular ROS generation in BSA–GNC-treated microorganisms was analyzed using confocal laser scanning microscopy

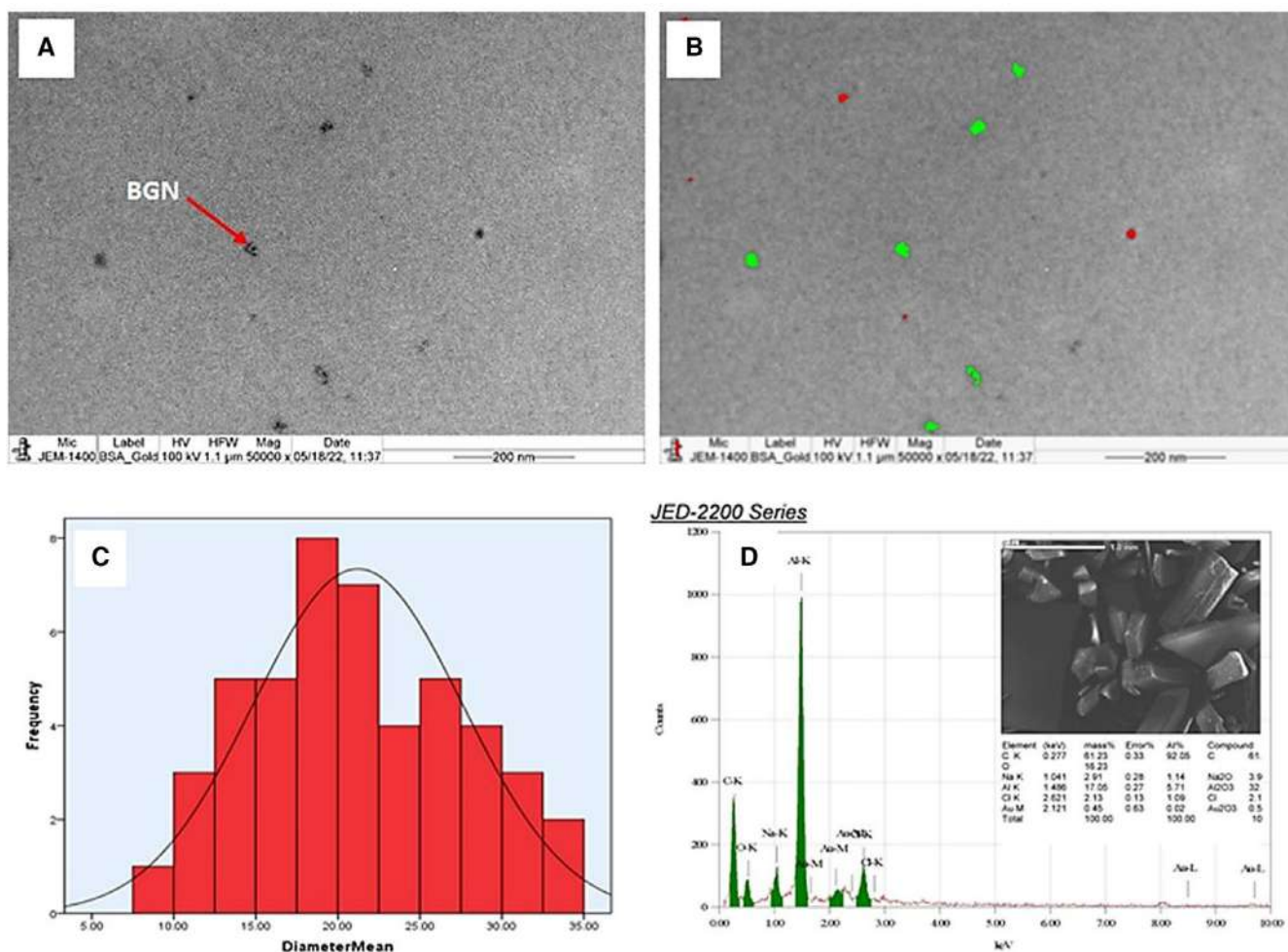


FIGURE 2 | Transmission and scanning electron microscopy analysis of BSA-GNCs. (A) Transmission electron micrograph showing BSA-GNCs; (B) color-coded image of (A), indicating particle size distribution; (C) graph depicting the particle size distribution; (D) scanning electron microscopy with EDX confirming elemental composition of the BSA-GNCs.

(CLSM 990, Zeiss, Germany). Briefly, 1 mL of LB medium containing approximately 10^7 CFU of bacterial cells was treated with BSA-GNCs at a final concentration of 40 $\mu\text{g/mL}$ and incubated for 12 h at 37°C. The cultures were then centrifuged at 6000 rpm for 10 min, and the supernatant was discarded. The bacterial pellets were washed with PBS and subsequently incubated in PBS containing 10 μM 2',7'-dichlorodihydrofluorescein diacetate ($\text{H}_2\text{DCFH-DA}$; C6827, Life Technologies, OR, USA) for 30 min at 37°C in the dark. After incubation, excess fluorescent probe was removed by washing the cells three times with PBS. A small volume of the labeled bacterial suspension was placed on glass slides, mounted with cover slips using appropriate mounting medium, and examined under a CLSM (CLSM 990, Zeiss, Germany). Fluorescence images were captured at an excitation wavelength of 485–504 nm and an emission wavelength of 525–535 nm using a Rolera QImaging camera. Image acquisition and quantification were performed using Zeiss Zen Lite software (version 3.11).

2.11 | TEM Analysis

Bacterial strains were cultured overnight (16 h) in 5 mL of nutrient agar at 37°C. The cultures were then transferred into separate test

tubes containing LB broth and grown to a final concentration of approximately 10^7 CFU/mL. Each bacterial culture was divided into two equal portions: One served as the untreated control, and the other was treated with 40 $\mu\text{g}/\mu\text{L}$ BSA-GNCs. Both treated and untreated cultures were incubated at 37°C for 24 h. Following incubation, the cultures were transferred into Eppendorf tubes and centrifuged at 6000 rpm for 10 min to obtain bacterial pellets. The collected pellets were processed for TEM analysis. Samples were fixed in 2.5% glutaraldehyde prepared in 0.1 M phosphate buffer (pH 7.4) for 2 h at 4°C, followed by post-fixation in 1% osmium tetroxide for 1 h. After fixation, the pellets were washed three times with distilled water (10 min each) and dehydrated through a graded ethanol series (50%, 70%, 90%, and 100%), followed by 100% acetone for 15 min each. Dehydrated samples were infiltrated with Spurr resin at ratios of 1:1 (resin:acetone) for 1 h and 2:1 (resin:acetone) for 2 h, followed by 100% resin infiltration (3×8 h). The infiltrated samples were polymerized in Eppendorf tubes at 70°C for 8 h to form resin blocks.

Five replicates were prepared for both untreated and BSA-GNC-treated bacterial samples. The polymerized resin blocks were sectioned into ultrathin sections (approximately 75 nm) using an

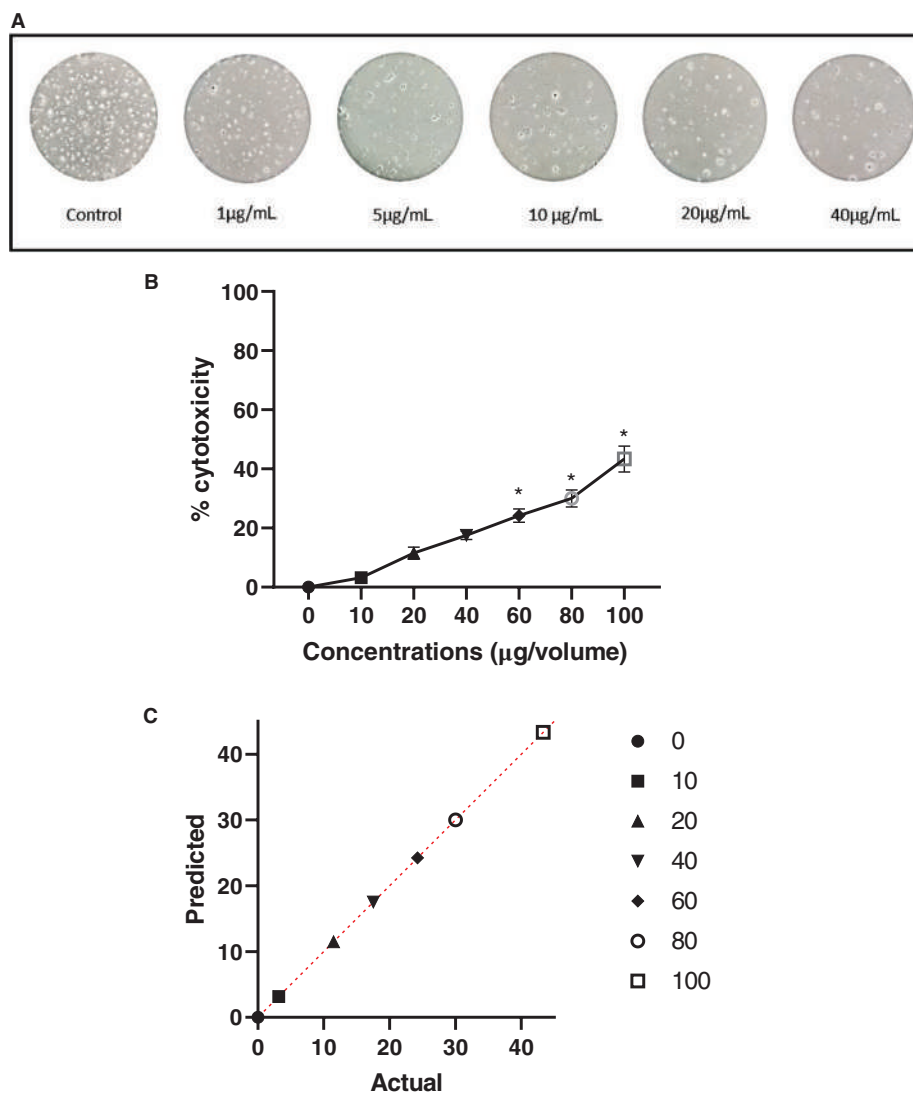


FIGURE 3 | Cytotoxicity of BSA-GNCs in HaCaT cells determined by MTT assay after 24 h incubation. (A) Representative images showing HaCaT cell morphology in the control and after treatment with 1–40 µg/µL BSA-GNCs for 24 h; (B and C) graphs representing percentage cytotoxicity in a concentration-dependent manner. Data are shown as mean ± SE ($n = 6$, each concentration assessed in triplicate, experiment repeated twice). Statistical analysis by the Mann–Whitney unpaired t -test; $p < 0.01$, indicated by *.

RMC Ultracut microtome. Sections were collected on 200-mesh copper grids and stained with 2% uranyl acetate and lead citrate. The ultrastructural features of bacteria were examined using a TEM (JEOL 1400, Tokyo, Japan). Digital images were captured using a bottom-mounted 15-megapixel Quemesa camera and analyzed with iTEM software.

2.12 | Statistical Analysis

All experimental data are presented as the mean ± standard error (SE) from at least three independent experiments. Statistical analyses were performed using GraphPad Prism software (version 8.2; GraphPad Software, San Diego, CA, USA). Differences between experimental groups were evaluated using the Mann–Whitney unpaired t -test for multiple comparisons. p values of 0.01, 0.001, and 0.0001 were considered statistically significant and are denoted as *, **, and ***, respectively, compared to the untreated bacterial control group.

3 | Results

3.1 | Characterization of BSA-GNCs

UV–spectrofluorimetric analysis of the synthesized BSA-GNCs exhibited a distinct fluorescence emission peak at 500 nm (Figure 1D), confirming the successful formation of gold nanoclusters that emitted characteristic red autofluorescence under UV illumination (Figure 1C). DLS and zeta potential analyses revealed that the BSA-GNCs possessed an average hydrodynamic size distribution peak and a negative surface charge of -8.29 mV (Figure 1E), indicating good colloidal stability. FTIR spectroscopy further confirmed the presence of major functional groups associated with BSA capping (Figure 1F). The FTIR spectrum displayed sharp absorption peaks between 400 and 4000 cm^{-1} , corresponding to characteristic functional vibrations at 598.33, 1102.79, 1261.21, 1637.84, 2923.54, and 3430.76 cm^{-1} , which represent C = O, phenolic, PO_2 , N–H, C–H, and O–H groups, respectively.

TEM images showed that the BSA–GNCs were well-dispersed, forming small clusters with variable diameters (Figure 2A,B). The mean particle diameter was 22.72 ± 0.93 nm, with a normal distribution pattern (Figure 2C). SEM coupled with EDX analysis confirmed the uniform distribution of BSA–GNCs (Figure 2D). The EDX spectrum exhibited a prominent Au–M peak at 2.12 keV, verifying the presence of gold and indicating efficient surface coating of Au atoms with BSA molecules.

3.2 | Cytotoxicity Assessment of BSA–GNCs

The cytotoxic potential of the synthesized BSA–GNCs was evaluated in cultured HaCaT skin keratinocytes. Figure 3 illustrates the dose-dependent cytotoxicity profile of BSA–GNCs across various concentrations. Representative microscopic images of HaCaT cells treated with 1–40 $\mu\text{g}/\mu\text{L}$ of BSA–GNCs are shown in Figure 3A. As depicted in Figure 3B,C, exposure to BSA–GNCs at concentrations ranging from 1 to 40 $\mu\text{g}/\mu\text{L}$ resulted in minimal cytotoxicity (less than 20%), showing no significant difference compared to untreated control cells. However, at higher concentrations (60, 80, and 100 $\mu\text{g}/\mu\text{L}$), a significant increase in cytotoxicity (greater than 40%, $p < 0.01$) was observed after 24 h of exposure. On the basis of these findings, 40 $\mu\text{g}/\mu\text{L}$ was considered an optimal, nontoxic concentration and was selected for subsequent experiments.

3.3 | Antibacterial Activity of BSA–GNCs

Treatment with 40 $\mu\text{g}/\mu\text{L}$ of BSA–GNCs exhibited significant antibacterial activity against all tested bacterial strains. The maximum zones of inhibition observed after 24 h of incubation were 28 ± 2.44 mm for *K. pneumoniae*, 27.5 ± 2.45 mm for *S. aureus*, 31.5 ± 1.91 mm for *P. aeruginosa*, and 29.75 ± 2.50 mm for *E. faecalis* (Figure 4A–E). In comparison, treatment with 20 $\mu\text{g}/\mu\text{L}$ of PS produced inhibition zones of 32 ± 2.48 , 33 ± 1.80 , 37 ± 2.16 , and 39.33 ± 1.80 mm, respectively. Although the PS-treated group exhibited slightly higher inhibition zones than the BSA–GNC-treated group. The antibacterial performance of BSA–GNCs was further evaluated relative to the control (0.9% saline), BSA, and gold ion (Au) solutions, confirming that the observed activity was primarily attributed to the synthesized nanoclusters (Figure 4A–E).

3.4 | Ultrastructural Analysis of Bacteria Treated With BSA–GNCs

TEM was used to compare the ultrastructural morphology of untreated and BSA–GNC-treated bacteria. Untreated *K. pneumoniae* cells were uniformly distributed and contained dense cytoplasm with numerous electron-dense ribosomes (Figure 5.1A). The cytoplasm was enclosed by a well-defined plasma membrane and cell wall, both covered by a thin biofilm layer (Figure 5.1B–D). In contrast, BSA–GNC-treated *K. pneumoniae* cells exhibited distinct cytoplasmic vacuolation (Figure 5.2A,B), with most cross-sections showing shrunken and degenerated cytoplasm (Figure 5.2C–F).

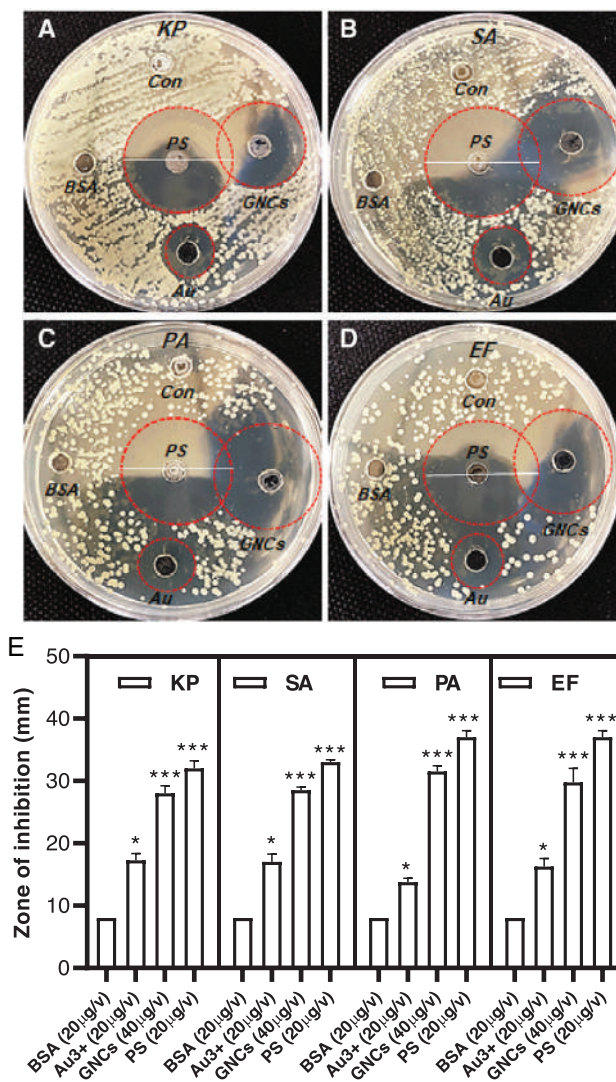


FIGURE 4 | Antibacterial activity of BSA–GNCs against antibiotic-resistant and non-resistant bacteria. (A–D) Agar plates showing bacterial growth inhibition after 24 h treatment with BSA (20 $\mu\text{g}/\mu\text{L}$), Au (20 $\mu\text{g}/\mu\text{L}$), BSA–GNCs (40 $\mu\text{g}/\mu\text{L}$), and penicillin–streptomycin (PS; 20 $\mu\text{g}/\mu\text{L}$). Red circles indicate zones of inhibition; (E) graphical representation of inhibition zones for each treatment group. Data are mean \pm SE ($n = 6$, each concentration assessed in triplicate, experiment repeated twice). Statistical analysis by the Mann–Whitney unpaired t -test; $p < 0.01$ compared to BSA and Au groups.

Untreated *S. aureus* formed compact clusters and exhibited an electron-dense cytoplasm surrounded by a thick biofilm (Figure 5.3A–D). Upon exposure to BSA–GNCs, *S. aureus* cells displayed severe structural damage, including vacuolation and cytoplasmic degeneration (Figure 5.4A–D). Many bacterial cells exhibited shrunken cytoplasm or remnants of intracellular content (Figure 5.4E,F).

Similarly, untreated *P. aeruginosa* cells exhibited a dense cytoplasm bounded by an intact plasma membrane, cell wall, and biofilm (Figure 5.5A–D). Following BSA–GNC treatment, *P. aeruginosa* cells displayed extensive degeneration and cytoplasmic shrinkage (Figure 5.6A,B), with many cells showing disorganized or collapsed cytoplasmic remnants (Figure 5.6C–F).

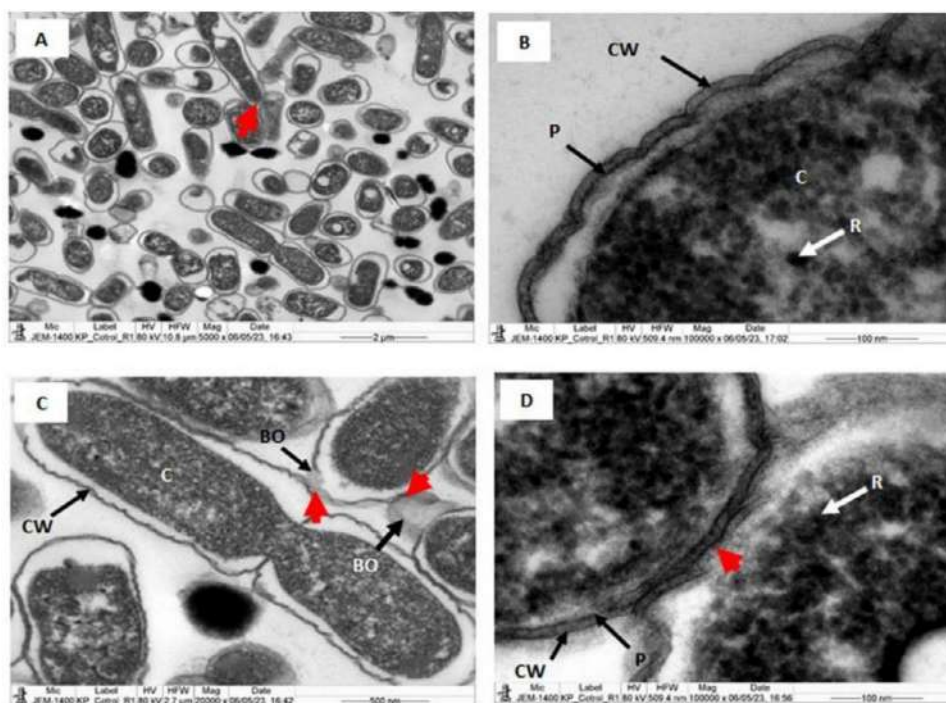


FIGURE 5 | Ultrastructural analysis of untreated and BSA-GNC-treated bacterial strains by electron microscopy. **5.1 (A–D)** Untreated *Klebsiella pneumoniae* showing dense cytoplasm and biofilm coating. **5.2 (A–F)** BSA-GNC-treated *K. pneumoniae* showing vacuolated cytoplasm, degenerated cytoplasmic contents, and disrupted membranes. **5.3 (A–D)** Untreated *Staphylococcus aureus* displaying clustered cells with electron-dense cytoplasm, intact plasma membrane, cell wall, and biofilm. **5.4 (A–F)** BSA-GNC-treated *S. aureus* showing degenerated membranes, cytoplasmic shrinkage, and vacuolization. **5.5 (A–D)** Untreated *Pseudomonas aeruginosa* with dense cytoplasm, intact membranes, and biofilm coating. **5.6 (A–F)** BSA-GNC-treated *P. aeruginosa* showing cytoplasmic degeneration, membrane folding, and vacuolated structures. **5.7 (A–F)** Untreated and BSA-GNC-treated *Enterococcus faecalis*; untreated bacteria fused via biofilm, while treated bacteria displayed shrunken cytoplasm, broken cell walls, and vacuolization. S = nucleoid strands, red arrow = fusion of bacteria. BO, biofilm; CW, cell wall; DC, degenerated cytoplasm; P, plasma membrane; RC, remnant cytoplasm; SC, shrunken cytoplasm.

The ultrastructure of untreated *E. faecalis* resembled that of *S. aureus*, displaying an electron-dense cytoplasm surrounded by a plasma membrane, cell wall, and a prominent biofilm layer (Figure 5.7A,B). Treatment with BSA-GNCs caused pronounced morphological damage, including cytoplasmic shrinkage and degradation of the cell wall and membrane disintegrates (Figure 5.7C–F).

3.5 | Quantification of Biofilm Inhibition and Bacterial Degeneration

Biofilm formation was assessed both qualitatively (Figure 6A,B) and quantitatively (Figure 6C,D) using crystal violet staining. Visual observations from the top-down view of the microtiter plates revealed substantial biofilm formation in untreated bacterial cultures at 24 and 48 h (Figure 6B). The extent of biofilm formation varied among bacterial species, depending on motility and adhesion properties, as evident from the dense colonies and adherent layers observed around the microplate wells (Figure 6A).

Quantitative assessment based on the ratio of crystal violet absorbance at 550 nm to culture absorbance at 600 nm revealed a significant increase in biofilm formation in untreated bacteria over time (Figure 6C). In contrast, BSA-GNC-treated bacteria

(40 µg/µL) exhibited a significant reduction in biofilm density at 48 h compared to 24 h (Figure 6D). These results indicate that BSA-GNCs effectively inhibit bacterial biofilm formation and promote structural degeneration in both Gram-positive and Gram-negative species.

3.6 | Intracellular ROS Generation in BSA-GNC-Treated Bacteria

An in vitro assay was performed to further elucidate the intracellular ROS generation induced by BSA-GNCs in bacterial cells. CLSM imaging (Figure 7.1A–H) clearly distinguished between untreated and BSA-GNC-treated bacteria. In comparison to the untreated groups (Figure 7.1A,C,E,G), BSA-GNC-treated bacteria (Figure 7.1B,D,F,H) exhibited a markedly higher intensity of green fluorescence, indicating increased ROS production.

Similarly, mean fluorescence intensity spectral distribution analysis confirmed these findings (Figure 7.2A–H). The BSA-GNC-treated bacteria displayed pronounced mean green fluorescence intensities (Figure 7.2B,D,F,H), whereas less fluorescence intensity was observed in untreated cells (Figure 7.2A,C,E,G). These results collectively demonstrate that exposure to BSA-GNCs induces significant ROS accumulation within bacterial cells, ultimately leading to oxidative stress-mediated cell death.

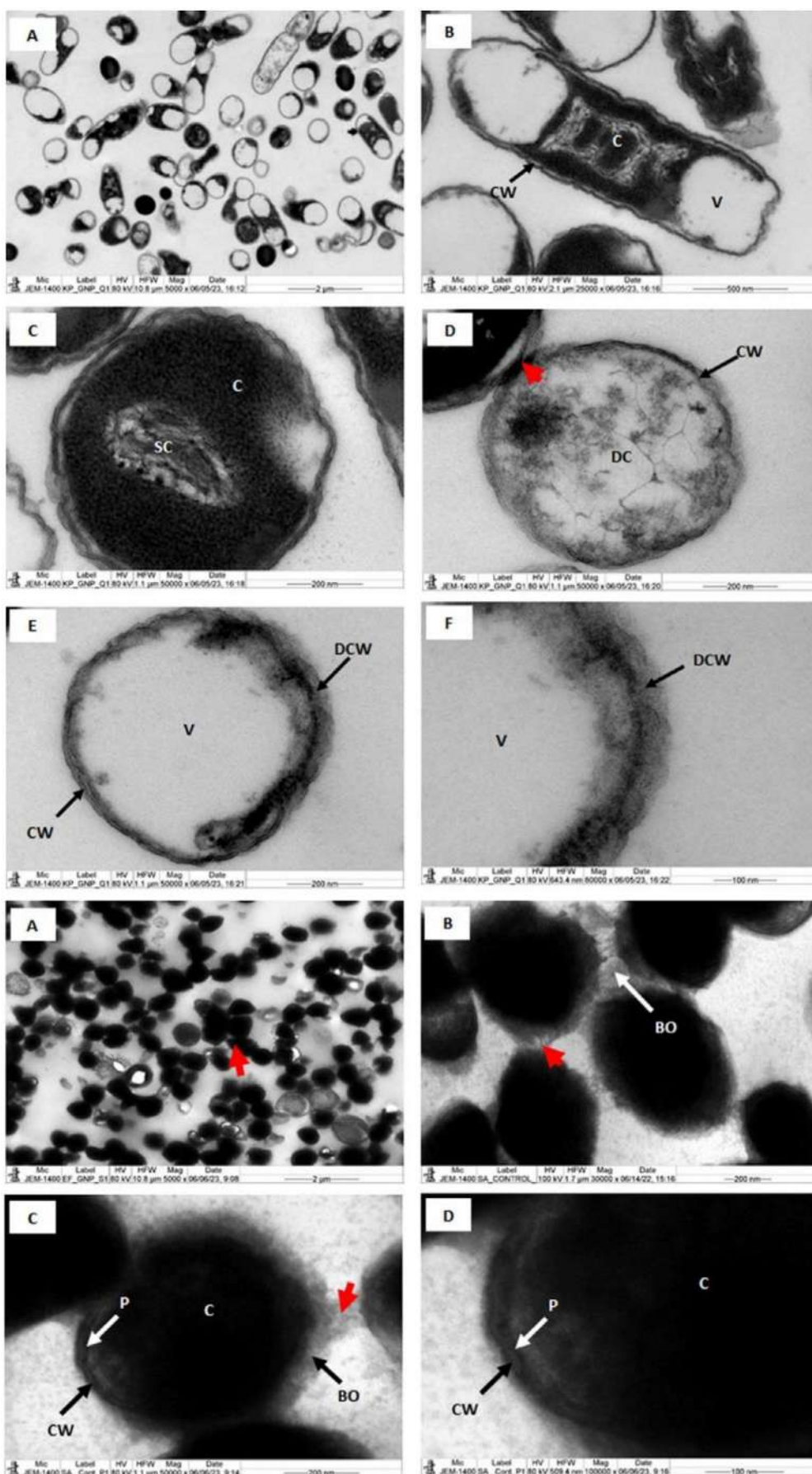


FIGURE 5 | (Continued)

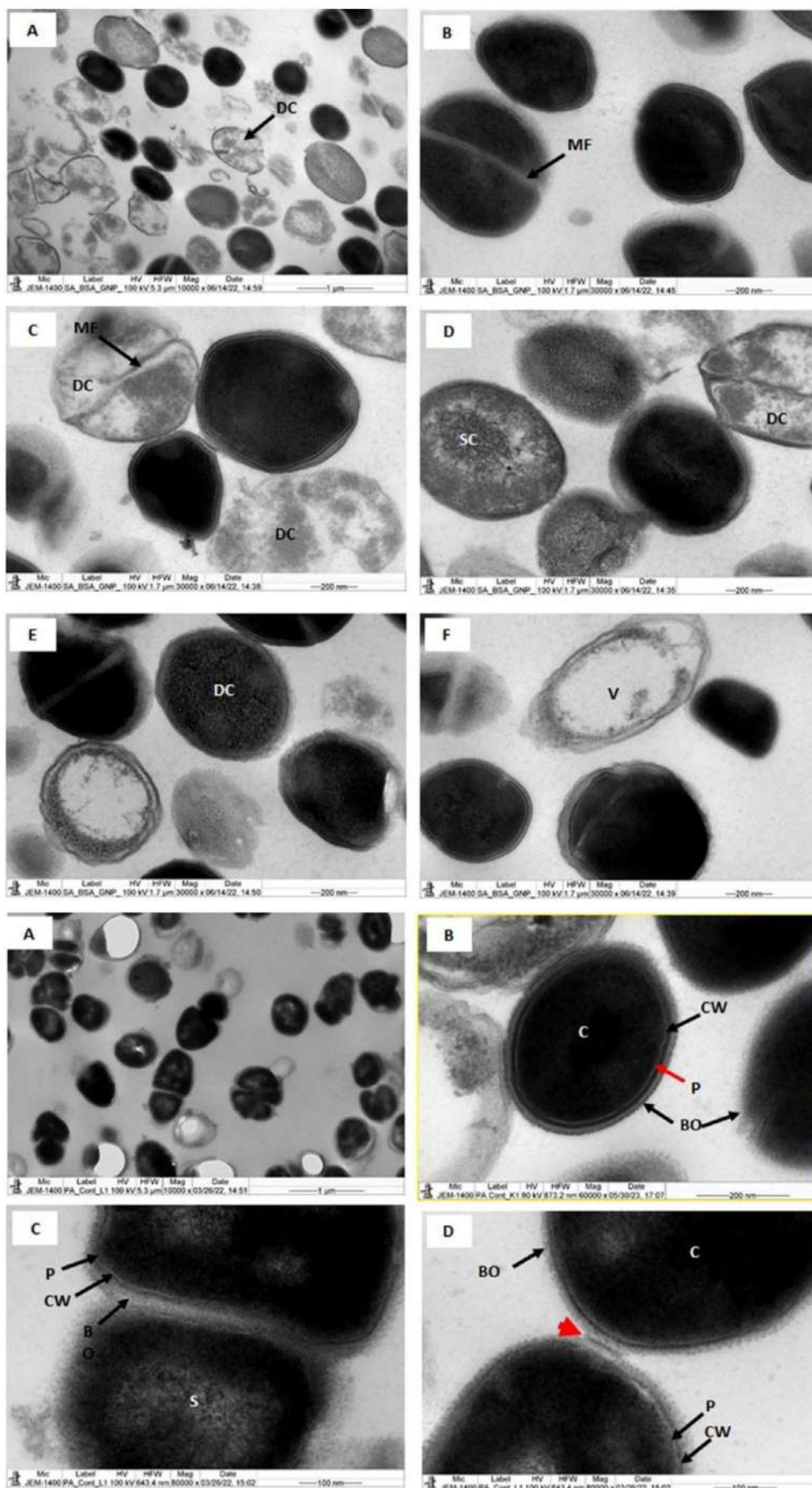


FIGURE 5 | (Continued)

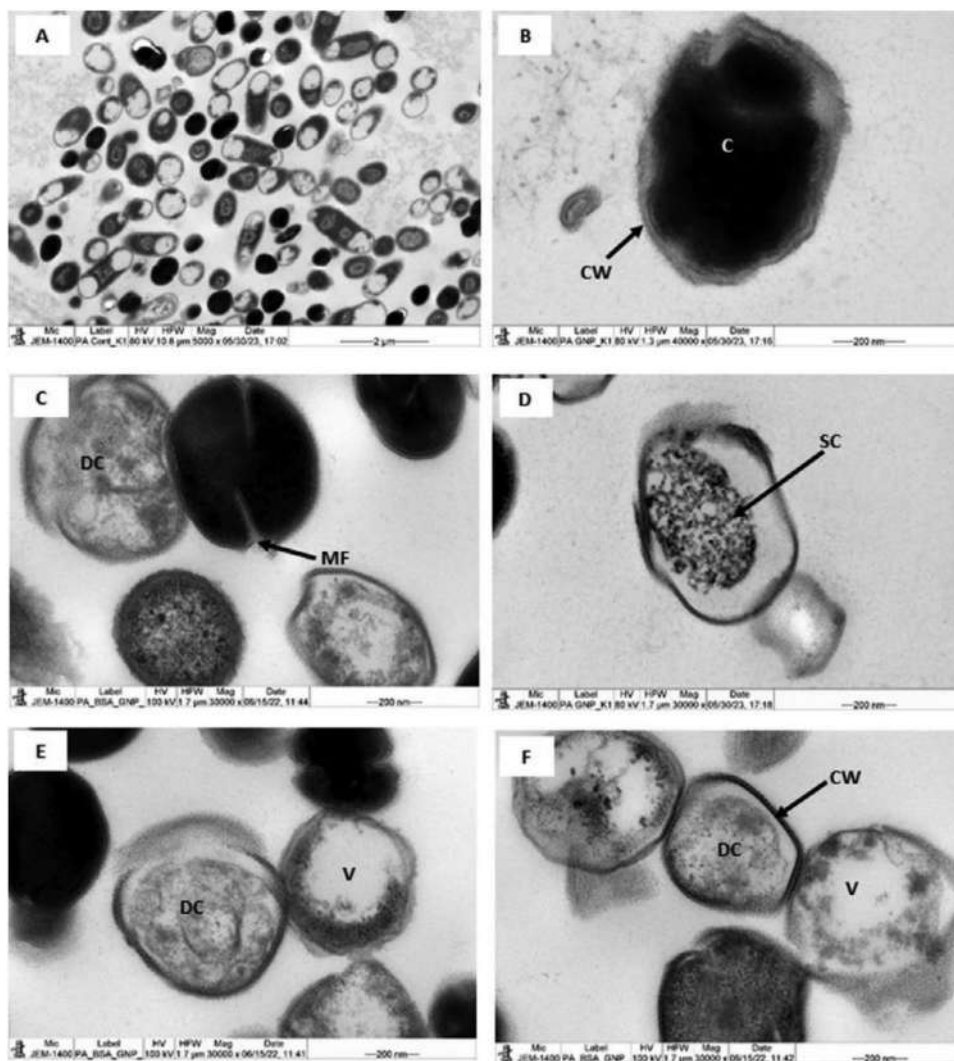


FIGURE 5 | (Continued)

4 | Discussion

The present study investigated the effects of BSA-GNCs on the susceptibility of antibiotic-resistant and non-resistant bacterial strains, as well as their influence on biofilm formation. Earlier, Housni et al. reported that BSA-capped gold nanoparticles were monodispersed and stabilized through BSA crosslinkages compared with uncapped gold nanoparticles [23]. In the current study, successfully synthesized BSA-GNCs were characterized by UV spectrofluorimetry, showing an emission peak at 500 nm with red fluorescence, consistent with previous reports [24]. Similarly, Lopez-Miranda et al. observed that increasing the concentration of BSA-GNCs to 3 mM enhanced the gold nanoparticle peak at 540 nm, confirming GNC formation [25].

FTIR analysis in this study revealed distinct peaks at 1637.84, 1102.79, and 3430.76 cm^{-1} , corresponding to C = O, C–H, and O–H functional groups, respectively, which is consistent with previous reports [26]. These functional groups are critical for capping and stabilizing AuNPs. TEM analysis confirmed that the synthesized BSA-GNCs were homogeneous, non-aggregated,

and exhibited various morphologies (spherical and cluster's) with an average diameter of 22.7 nm, which aligns closely with previous findings (25.5 nm) [26, 27]. Bronze-Uhle et al. and Shankar et al. also reported similar BSA-AuNP morphologies and elemental confirmation through EDS peaks at approximately 2.1 keV [28, 29]. Our SEM-EDX analysis likewise demonstrated a uniform distribution of BSA-GNCs with a characteristic Au-M peak at 2.12 keV, verifying successful BSA coating [30]. DLS analysis indicated that the hydrodynamic diameter of BSA-GNCs was larger than the core particle size, likely due to ligand adsorption and formation of an electrical double layer around the particles [31].

Cytotoxicity evaluation using the MTT assay revealed that BSA-GNCs exhibited minimal toxicity toward HaCaT cells at concentrations up to 40 $\mu\text{g}/\mu\text{L}$, with cell viability exceeding 80%. However, concentrations above 60 $\mu\text{g}/\mu\text{L}$ induced significant cytotoxic effects ($p < 0.01$). This suggests that at lower doses, BSA-GNCs exert mild oxidative stress-mediated effects without triggering cell death, whereas higher concentrations elicit intrinsic toxicity, consistent with previous reports on gold nanoclusters [21].

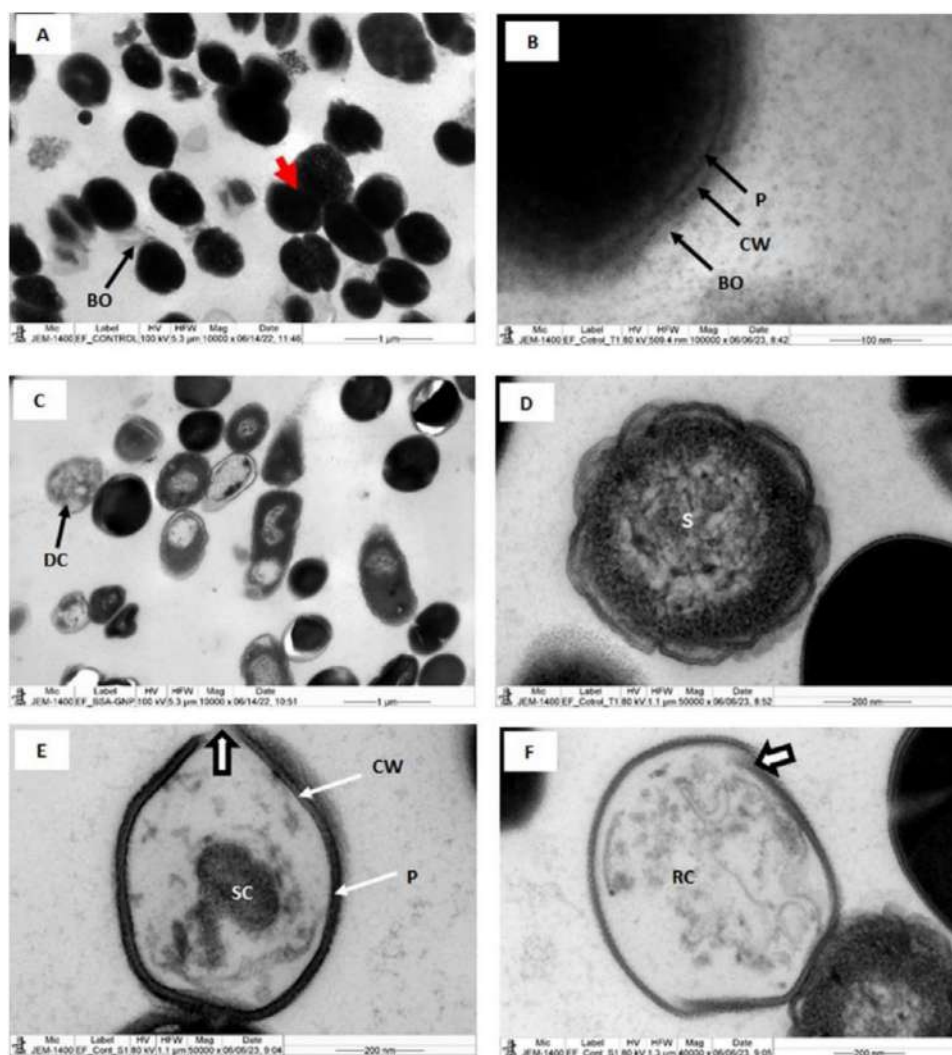


FIGURE 5 | (Continued)

Antibacterial assays demonstrated that 40 $\mu\text{g}/\mu\text{L}$ BSA-GNCs produced significant inhibition zones compared with BSA and Au alone, confirming their superior antibacterial efficacy. TEM ultrastructural analyses revealed severe bacterial damage, including cytoplasmic vacuolation, membrane shrinkage, and cell wall disruption, indicative of compromised integrity. Similar ultrastructural alterations have been observed following exposure to membrane-permeabilizing agents such as phenethyl alcohol and triethylsilanol [31–33]. Gold nanomaterials possess unique antibacterial advantages due to their tunable size, shape, and multivalent surface chemistry [34]. Their ability to adopt various morphologies—including spheres, rods, stars, and nanoclusters—enables controlled interactions with bacterial cell walls and biofilm matrices. The multivalent nature of AuNPs facilitates binding with multiple bacterial ligands, thereby enhancing antibacterial potency against both Gram-positive and Gram-negative species [35].

Our results demonstrated that BSA-GNCs effectively inhibited both resistant and non-resistant bacterial strains. The biofilm inhibition assay further confirmed that BSA-GNC treatment markedly reduced biofilm formation at both 24 and 48 h, as evidenced by crystal violet staining. The qualitative and quantitative

data were consistent, showing a pronounced reduction in biofilm density and coloration in treated groups. The spatial biofilm distribution differed across species: *K. pneumoniae* formed upper-surface aggregates, whereas *S. aureus*, *P. aeruginosa*, and *E. faecalis* developed denser, uniform biofilms across plate surfaces. All strains exhibited thinner biofilm layers at 48 h following BSA-GNC exposure, consistent with literature emphasizing the importance of initial microbial adherence in biofilm formation [36, 37].

BSA-GNCs likely inhibit biofilm development by impairing bacterial cell wall permeability and disrupting metabolic and signaling pathways essential for extracellular polymeric substance (EPS) synthesis. Previous studies have demonstrated that BSA-capped GNCs promote the generation of ROS, lipid peroxidation products such as malondialdehyde (MDA), and leakage of cytoplasmic proteins and sugars [34, 38, 39]. These effects collectively compromise bacterial envelope integrity and interfere with EPS assembly. The proposed antibacterial mechanism of BSA-GNCs involves their penetration through bacterial pores and efflux channels, resulting in the inhibition of EPS formation and biofilm development. Consequently, the bacterial plasma membrane retracts from the cell wall, creating electron-lucent

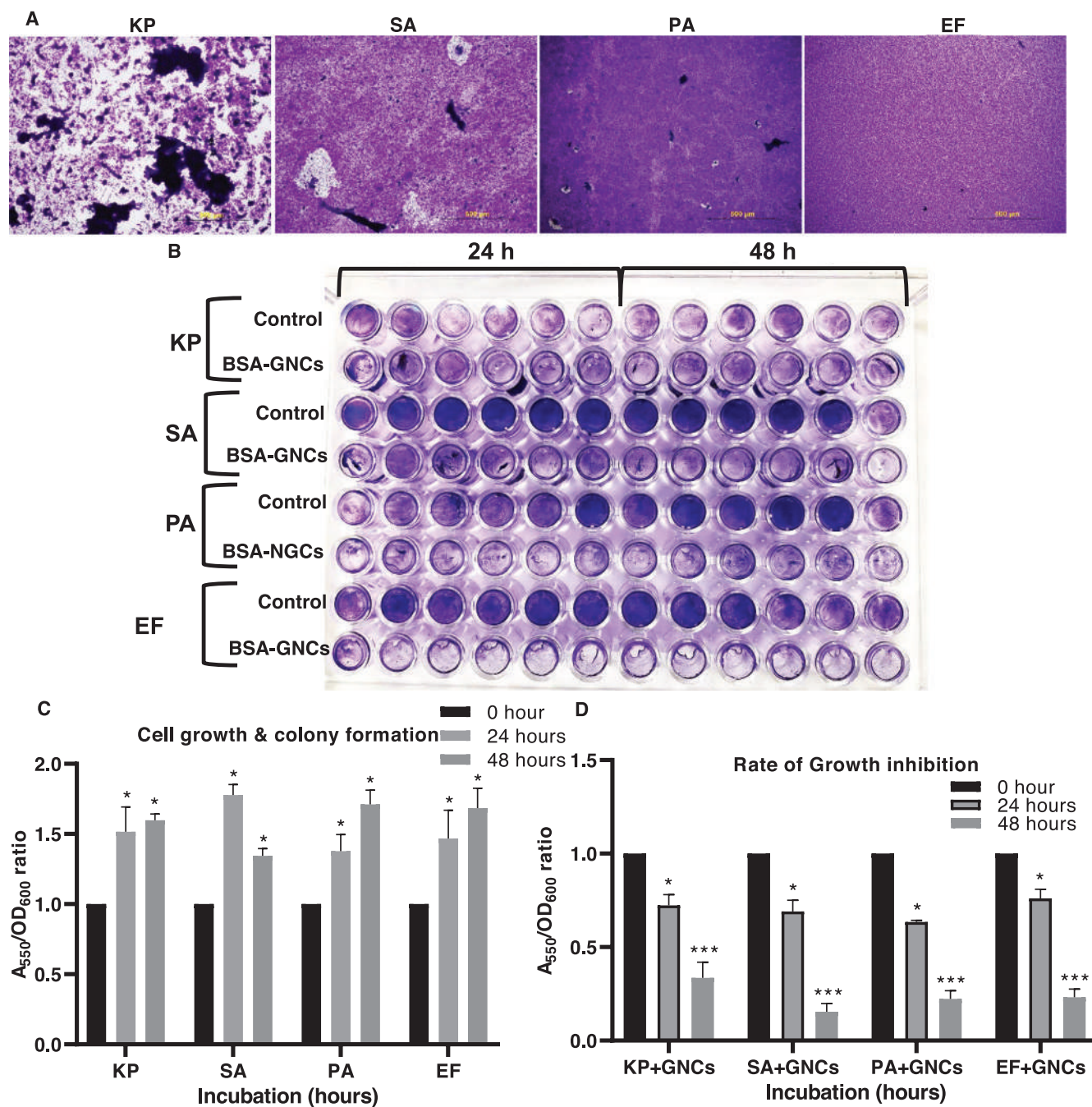


FIGURE 6 | Quantitative and qualitative assessment of biofilm formation in untreated and BSA-GNC-treated bacteria. (A) Photograph showing untreated bacterial biofilm formation at 24 h; (B) crystal violet staining of untreated and BSA-GNC-treated bacteria at 100× magnification; (C and D) quantitative biofilm formation in *Klebsiella pneumoniae*, *Staphylococcus aureus*, *Pseudomonas aeruginosa*, and *Enterococcus faecalis* at 24 and 48 h. (C) Untreated bacterial biofilm formation; (D) inhibition in BSA-GNC-treated bacteria. Data are mean ± SE ($n = 6$, triplicate per concentration). The Mann-Whitney unpaired t -test; $p < 0.01$ compared to control. BSA-GNC, bovine serum albumin-gold nanocluster.

spaces between these layers and leading to cytoplasmic degradation. The disintegration of cytoplasmic content and the disruption of structural integrity ultimately impair bacterial adhesion and colonization. These findings are consistent with previous reports, which demonstrated that functionally engineered materials can induce the loss of bacterial physical and mechanical stability [13, 40, 41]. Hence, the functionalized nanomaterials exhibited minimal adverse effects on mammalian cell viability, yet effectively inhibited bacterial adhesion and early biofilm formation.

This differential response highlights the selective antimicrobial potential of BSA-GNCs, supporting their suitability as promising candidates for anti-biofilm and surface-protective applications.

5 | Conclusion

This study demonstrates the antibacterial, anti-biofilm, and cytocompatible properties of BSA-GNCs; however, several limi-

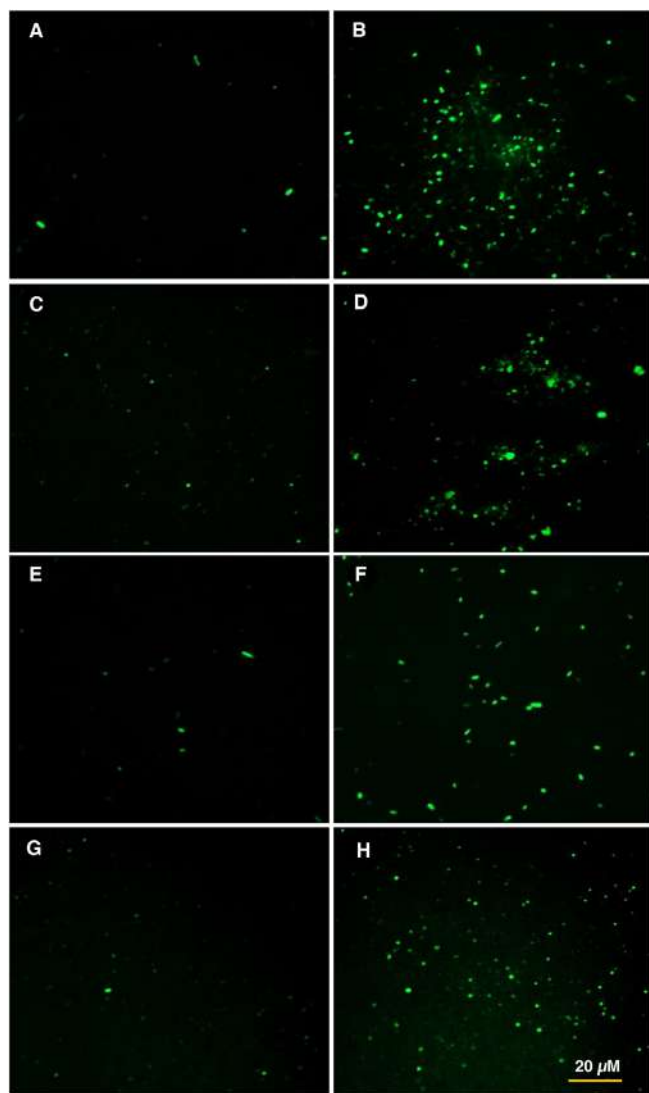


FIGURE 7 | *Confocal microscopy analysis of intracellular ROS generation in untreated and BSA-GNC-treated bacteria. 7.1 (A–H)* DCFH-DA-stained bacteria imaged after 12 h incubation at 400× magnification (scale bar = 20 μm); (A, C, E, G) untreated, (B, D, F, H) BSA-GNC-treated groups. **7.2 (A–H)** 3D spectral analysis of ROS accumulation quantified using Zen Lite 3.11 software. Green fluorescence indicates ROS-positive cells, which markedly increased in BSA-GNC-treated bacteria at 12 h.

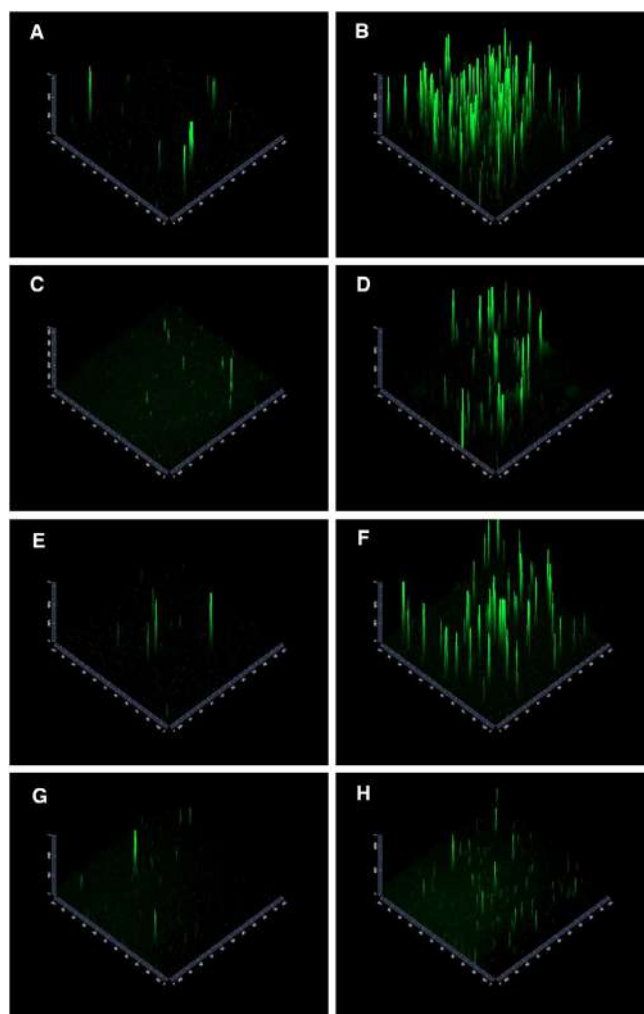


FIGURE 7 | (Continued)

tations should be noted. First, all experiments were performed in vitro, which cannot fully represent in vivo biological complexity, immune responses, or systemic toxicity. Mechanistic insights into how BSA-GNCs exert antimicrobial action remain incomplete, as pathways such as membrane disruption, cytosolic alterations, and quorum sensing interference were not extensively explored. Additionally, cytotoxicity was assessed using only one cell line (HaCaT), and long-term stability of the nanoclusters under physiological conditions was not evaluated.

Future studies should expand antibacterial testing to a broader range of MDR pathogens, and evaluating BSA-GNCs against mature and polymicrobial biofilms will enhance clinical relevance. Additionally, exploring formulation optimization, targeted delivery approaches, and potential synergistic effects with antibi-

otics could support translation of BSA-GNCs into practical biomedical applications.

Author Contributions

Mana A. Alanazi: methodology, software, validation, formal analysis, data curation, writing – original draft preparation, writing – review and editing. **Ramachandran Samivel:** conceptualization, methodology, software, validation, formal analysis, investigation, resources, data curation, writing – original draft preparation, writing – review and editing. **Turki Almubrad:** data curation, writing – original draft preparation, writing – review and editing, funding acquisition. **Adnan A. Khan:** methodology, software, validation, formal analysis. **Ali Masmali:** data curation, writing – original draft preparation, writing – review and editing. **Saud A. Alanazi:** resources, project administration, funding acquisition, writing – original draft preparation, writing – review and editing. **Saeed Akhtar:** conceptualization, methodology, software, validation, formal analysis, investigation, resources, data curation, writing – original draft preparation, writing – review and editing, visualization and supervision. All the authors have read and agreed to the published version of the manuscript.

Acknowledgments

The authors acknowledge the support received from the Ongoing Research Funding Program (ORF-RC-2025-1300), King Saud University, Riyadh, Saudi Arabia.

Consent

The authors have nothing to report.

Conflicts of Interest

The authors declare no conflicts of interest.

Data Availability Statement

The data supporting the findings of this study are available from the corresponding author upon reasonable request.

References

1. G. Mancuso, A. Midiri, E. Gerace, and C. Biondo, "Bacterial Antibiotic Resistance: The Most Critical Pathogens," *Pathogens* 10, no. 10 (2021): 1310, <https://doi.org/10.3390/pathogens10101310>.
2. S. McEwen and P. Collignon, "Antimicrobial Resistance: A One Health Perspective," *Microbiology Spectrum* 6 (2018): 521–547, <https://doi.org/10.1128/microbiolspec.arba-0009-2017>.
3. G. Mancuso, A. Midiri, E. Gerace, and C. Biondo, "Bacterial Antibiotic Resistance: The Most Critical Pathogens," *Pathogens* 10, no. 10 (2021): 1310, <https://doi.org/10.3390/pathogens10101310>.
4. A. R. Collaborators, "Global Burden of Bacterial Antimicrobial Resistance in 2019: A Systematic Analysis," *Lancet* 399, no. 10325 (2022): P629–P655, [https://doi.org/10.1016/S0140-6736\(21\)02724-0](https://doi.org/10.1016/S0140-6736(21)02724-0).
5. S. J. Post, J. A. Shapiro, and W. M. Wuest, "Connecting Iron Acquisition and Biofilm Formation in the ESKAPE Pathogens as a Strategy for Combating Antibiotic Resistance," *Medicinal Chemistry Communications* 10 (2019): 505–512, <https://doi.org/10.1039/C9MD00032A>.
6. R. Y. Pelgrift and A. J. Friedman, "Nanotechnology as a Therapeutic Tool to Combat Microbial Resistance," *Advanced Drug Delivery Reviews* 65 (2013): 1803–1815, <https://doi.org/10.1016/j.addr.2013.07.011>.
7. X. Zhan, J. Yan, H. Tang, D. Xia, and H. Lin, "Antibacterial Properties of Gold Nanoparticles in the Modification of Medical Implants: A Systematic Review," *Pharmaceutics* 14, no. 12 (2022): 2654, <https://doi.org/10.3390/pharmaceutics14122654>.
8. A. Abdal Dayem, M. K. Hossain, S. B. Lee, et al., "The Role of Reactive Oxygen Species (ROS) in the Biological Activities of Metallic Nanoparticles," *International Journal of Molecular Sciences* 18, no. 1 (2017): 120, <https://doi.org/10.3390/ijms18010120>.
9. Y. S. Huang, J. T. Wang, H. M. Tai, P. C. Chang, H. C. Huang, and P. C. Yang, "Metal Nanoparticles and Nanoparticle Composites Are Effective Against *Haemophilus influenzae*, *Streptococcus pneumoniae*, and Multidrug-Resistant Bacteria," *Journal of Microbiology, Immunology, and Infection* 55, no. 4 (2022): 708–715, <https://doi.org/10.1016/j.jmii.2022.05.003>.
10. T. Y. Yang, Y. J. Hsieh, P. L. Lu, et al., "In Vitro and In Vivo Assessments of Inspired Ag/80S Bioactive Nanocomposites Against Carbapenem-Resistant *Klebsiella pneumoniae*," *Materials Science & Engineering C, Materials for Biological Applications* 125 (2021): 112093, <https://doi.org/10.1016/j.msec.2021.112093>.
11. V. Kattumuri, K. Katti, S. Bhaskaran, et al., "Gum Arabic as a Phytochemical Construct for the Stabilization of Gold Nanoparticles: In Vivo Pharmacokinetics and X-Ray-Contrast-Imaging Studies," *Small (Weinheim an Der Bergstrasse, Germany)* 3, no. 2 (2007): 333–341, <https://doi.org/10.1002/sml.200600427>.
12. G. Wang, H. Feng, W. Jin, et al., "Long-Term Antibacterial Characteristics and Cytocompatibility of Titania Nanotubes Loaded With Au Nanoparticles Without Photocatalytic Effects," *Applied Surface Science* 414 (2017): 230–237, <https://doi.org/10.1016/j.apsusc.2017.04.053>.
13. C. Mutalik, M. Saukani, M. Khafid, et al., "Gold-Based Nanostructures for Antibacterial Application," *International Journal of Molecular Sciences* 24, no. 12 (2023): 10006, <https://doi.org/10.3390/ijms241210006>.
14. T. Wu, K. Chen, W. Lai, et al., "Bovine Serum Albumin-Gold Nanoclusters Protein Corona Stabilized Polystyrene Nanoparticles as Dual-Color Fluorescent Nanoprobes for Breast Cancer Detection," *Biosensors & Bioelectronics* 215 (2022): 114575, <https://doi.org/10.1016/j.bios.2022.114575>.
15. T. T. Nguyen, D. Nguyen Thi Kieu, H. V. Bui, L. Le Thi Ngoc, and V. H. Nguyen, "Enhancing Control in Spatial Atomic Layer Deposition: Insights Into Precursor Diffusion, Geometric Parameters, and CVD Mitigation Strategies," *Nanotechnology* 35, no. 20 (2024): 205601, <https://doi.org/10.1088/1361-6528/ad28d6>.
16. V. Jain, S. Bhagat, and S. Singh, "Bovine Serum Albumin Decorated Gold Nanoclusters: A Fluorescence-Based Nanoprobe for Detection of Intracellular Hydrogen Peroxide," *Sensors and Actuators B: Chemical* 327 (2021): 128886, <https://doi.org/10.1016/j.snb.2020.128886>.
17. R. Javed, M. Zia, S. Naz, S. O. Aisida, N. U. Ain, and Q. Ao, "Role of Capping Agents in the Application of Nanoparticles in Biomedicine and Environmental Remediation: Recent Trends and Future Prospects," *Journal of Nanobiotechnology* 18, no. 1 (2020): 172, <https://doi.org/10.1186/s12951-020-00704-4>.
18. K. Bolaños, M. J. Kogan, and E. Araya, "Capping Gold Nanoparticles With Albumin to Improve Their Biomedical Properties," *International Journal of Nanomedicine* 14 (2019): 6387–6406, <https://doi.org/10.2147/IJN.S210992>.
19. J. Simon, S. Udayan, E. S. Bindia, S. G. Bhat, V. P. N. Nampoori, and M. Kailasnath, "Optical Characterization and Tunable Antibacterial Properties of Gold Nanoparticles With Common Proteins," *Analytical Biochemistry* 612 (2021): 113975, <https://doi.org/10.1016/j.ab.2020.113975>.
20. R. Purohit and S. Singh, "Fluorescent Gold Nanoclusters for Efficient Cancer Cell Targeting," *International Journal of Nanomedicine* 13 (2018): 15–17, <https://doi.org/10.2147/IJN.S125003>.
21. C. R. Lillo, M. N. Calienni, B. Rivas Aiello, et al., "BSA-Capped Gold Nanoclusters as Potential Theragnostic for Skin Diseases: Photoactivation, Skin Penetration, In Vitro, and In Vivo Toxicity," *Materials Science & Engineering C, Materials for Biological Applications* 112 (2020): 110891, <https://doi.org/10.1016/j.msec.2020.110891>.
22. G. A. O'Toole, "Microtiter Dish Biofilm Formation Assay," *Journal of Visualized Experiments: JoVE* 47 (2011): 2437, <https://doi.org/10.3791/2437>.
23. A. Housni, M. Ahmed, S. Liu, and R. Narain, "Monodisperse Protein Stabilized Gold Nanoparticles via a Simple Photochemical Process," *Journal of Physical Chemistry C* 112 (2008): 12282–12290, <https://doi.org/10.1021/jp803890a>.
24. K. Zheng, M. I. Setyawati, D. I. Leong, and J. Xie, "Surface Ligand Chemistry of Gold Nanoclusters Determines Their Antimicrobial Ability," *Chemistry of Materials* 30 (2018): 2800–2808, <https://doi.org/10.1021/acs.chemmater.8b00667>.
25. J. L. Lopez-Miranda, R. Esparza, G. Rosas, R. Perez, and M. Estevez-Gonzalez, "Catalytic and Antibacterial Properties of Gold Nanoparticles Synthesized by a Green Approach for Bioremediation Applications," *3 Biotech* no. 4 (2019): 135, <https://doi.org/10.1007/s13205-019-1666-z>.
26. A. Folorunso, S. Akintelu, A. K. Oyebamiji, et al., "Biosynthesis, Characterization and Antimicrobial Activity of Gold Nanoparticles From Leaf Extracts of *Annona muricata*," *Journal of Nanostructure in Chemistry* 9 (2019): 111–117, <https://doi.org/10.1007/s40097-019-0301-1>.
27. I. Matei, C. M. Buta, I. M. Turcu, D. Culita, C. Munteanu, and G. Ionita, "Formation and Stabilization of Gold Nanoparticles in Bovine Serum Albumin Solution," *Molecules* 24, no. 18 (2019): 3395, <https://doi.org/10.3390/molecules24183395>.
28. E. S. Bronze-Uhle, B. C. Costa, V. F. Ximenes, and P. N. Lisboa-Filho, "Synthetic Nanoparticles of Bovine Serum Albumin With Entrapped

- Salicylic Acid," *Nanotechnology Science and Applications* 10 (2016): 11–21, <https://doi.org/10.2147/NSA.S117018>.
29. S. Shankar, N. S. K. Gowthaman, and S. A. John, "Synthesis of Albumin Capped Gold Nanoparticles and Their Direct Attachment on Glassy Carbon Electrode for the Determination of Nitrite Ion," *Journal of Electroanalytical Chemistry* 828 (2018): 33–40, <https://doi.org/10.1016/j.jelechem.2018.09.030>.
30. G. Wang, C. Yan, S. Gao, and Y. Liu, "Surface Chemistry of Gold Nanoparticles Determines Interactions With Bovine Serum Albumin," *Materials Science & Engineering C, Materials for Biological Applications* 103 (2019): 109856, <https://doi.org/10.1016/j.msec.2019.109856>.
31. J. Corre, J. J. Lucchini, G. M. Mercier, and A. Cremieux, "Antibacterial Activity of Phenethyl Alcohol and Resulting Membrane Alterations," *Research in Microbiology* 141, no. 4 (1990): 483–497, [https://doi.org/10.1016/0923-2508\(90\)90074-Z](https://doi.org/10.1016/0923-2508(90)90074-Z).
32. Y. Kim, S. Farrah, and R. H. Baney, "Membrane Damage of Bacteria by Silanols Treatment," *Electronic Journal of Biotechnology* 10 no. 2 (2007), <https://doi.org/10.4067/S0717-34582007000200009>.
33. D. L. Veras, A. C. De Souza Lopes, G. Vaz Da Silva, et al., "Ultrastructural Changes in Clinical and Microbiota Isolates of *Klebsiella pneumoniae* Carriers of Genes blaSHV, blaTEM, blaCTX-M, or blaKPC When Subject to β -Lactam Antibiotics," *Scientific World Journal* 2015 (2015): 572128, <https://doi.org/10.1155/2015/572128>.
34. M. Okkeh, N. Bloise, E. Restivo, L. De Vita, P. Pallavicini, and L. Visai, "Gold Nanoparticles: Can They Be the Next Magic Bullet for Multidrug-Resistant Bacteria?," *Nanomaterials* 11, no. 2 (2021): 312, <https://doi.org/10.3390/nano11020312>.
35. R. Kamimura, H. Kanematsu, A. Ogawa, et al., "Quantitative Analyses of Biofilm by Using Crystal Violet Staining and Optical Reflection," *Materials* 15 (2022): 6727, <https://doi.org/10.3390/ma15196727>.
36. M. Borowicz, D. M. Krzyżanowska, and S. Jafra, "Crystal Violet-Based Assay for the Assessment of Bacterial Biofilm Formation in Medical Tubing," *Journal of Microbiological Methods* 204 (2023): 106656, <https://doi.org/10.1016/j.mimet.2022.106656>.
37. X. Shao, Y. Xie, Y. Zhang, and X. Deng, "Biofilm Formation Assay in *Pseudomonas syringae*," *Bio-Protocol* 9, no. 10 (2019): e3237, <https://doi.org/10.21769/BioProtoc.3237>.
38. Y. G. Yuan, Q. L. Peng, and S. Gurunathan, "Effects of Silver Nanoparticles on Multiple Drug-Resistant Strains of *Staphylococcus aureus* and *Pseudomonas aeruginosa* From Mastitis-Infected Goats: An Alternative Approach for Antimicrobial Therapy," *International Journal of Molecular Sciences* 18, no. 3 (2017): 569, <https://doi.org/10.3390/ijms18030569>.
39. M. Mmola, M. L. Roes-Hill, K. Durrell, et al., "Enhanced Antimicrobial and Anticancer Activity of Silver and Gold Nanoparticles Synthesised Using *Sargassum incisifolium* Aqueous Extracts," *Molecules* 21, no. 12 (2016): 1633, <https://doi.org/10.3390/molecules21121633>.
40. Y. Tang, Y. Li, P. Chen, S. Zhong, and Y. Yang, "Nucleic Acid Aptamer-Based Sensors for Bacteria Detection: A Review," *BioEssays* 47, no. 3 (2025): e202400111, <https://doi.org/10.1002/bies.202400111>.
41. J. Chen, F. Chen, S. Peng, et al., "Effects of Artemisia Argyi Powder on Egg Quality, Antioxidant Capacity, and Intestinal Development of Roman Laying Hens," *Frontiers in Physiology* 13 (2022): 902568, <https://doi.org/10.3389/fphys.2022.902568>.